IVYSPRING INTERNATIONAL PUBLISHER

Theranostics

2018; 8(21): 5903-5914. doi: 10.7150/thno.27679

Research Paper

Dual-Modality ImmunoPET/Fluorescence Imaging of Prostate Cancer with an Anti-PSCA Cys-Minibody

Wenting K Tsai[1], Kirstin A Zettlitz[1], Richard Tavaré[1,2], Naoko Kobayashi[3], Robert E Reiter[3], Anna M Wu[1,4]✉

1. Crump Institute for Molecular Imaging, Department of Molecular and Medical Pharmacology, David Geffen School of Medicine, UC Los Angeles
2. Current address: Regeneron Pharmaceuticals, Inc., Tarrytown, New York
3. Department of Urology, David Geffen School of Medicine, UC Los Angeles
4. Current address: Department of Molecular Imaging and Therapy, Beckman Research Institute, City of Hope, Duarte

✉ Corresponding author: Anna M Wu, Department of Molecular Imaging and Therapy, Beckman Research Institute, City of Hope, 1500 E. Duarte Rd. Duarte, CA 91010, USA. Tel: 1 (626) 218-8051; email: awu@coh.org

Received: 2018.06.05; Accepted: 2018.09.04; Published: 2018.11.12

Abstract

Inadequate diagnostic methods for prostate cancer lead to over- and undertreatment, and the inability to intraoperatively visualize positive margins may limit the success of surgical resection. Prostate cancer visualization could be improved by combining the complementary modalities of immuno-positron emission tomography (immunoPET) for preoperative disease detection, and fluorescence imaging-guided surgery (FIGS) for real-time intraoperative tumor margin identification. Here, we report on the evaluation of dual-labeled humanized anti-prostate stem cell antigen (PSCA) cys-minibody (A11 cMb) for immunoPET/fluorescence imaging in subcutaneous and orthotopic prostate cancer models.

Methods: A11 cMb was site-specifically conjugated with the near-infrared fluorophore Cy5.5 and radiolabeled with ^{124}I or ^{89}Zr. ^{124}I-A11 cMb-Cy5.5 was used for successive immunoPET/fluorescence imaging of prostate cancer xenografts expressing high or moderate levels of PSCA (22Rv1-PSCA and PC3-PSCA). ^{89}Zr-A11 cMb-Cy5.5 dual-modality imaging was evaluated in an orthotopic model. *Ex vivo* biodistribution at 24 h was used to confirm the uptake values, and tumors were visualized by post-mortem fluorescence imaging.

Results: A11 cMb-Cy5.5 retained low nanomolar affinity for PSCA-positive cells. Conjugation conditions were established (dye-to-protein ratio of 0.7:1) that did not affect the biodistribution, pharmacokinetics, or clearance of A11 cMb. ImmunoPET using dual-labeled ^{124}I-A11 cMb-Cy5.5 showed specific targeting to both 22Rv1-PSCA and PC3-PSCA s.c. xenografts in nude mice. *Ex vivo* biodistribution confirmed specific uptake to PSCA-expressing tumors with 22Rv1-PSCA:22Rv1 and PC3-PSCA:PC3 ratios of 13:1 and 5.6:1, respectively. Consistent with the immunoPET, fluorescence imaging showed a strong signal from both 22Rv1-PSCA and PC3-PSCA tumors compared with non-PSCA expressing tumors. In an orthotopic model, ^{89}Zr-A11 cMb-Cy5.5 immunoPET was able to detect intraprostatically implanted 22Rv1-PSCA cells. Importantly, fluorescence imaging clearly distinguished the prostate tumor from surrounding seminal vesicles.

Conclusion: Dual-labeled A11 cMb specifically visualized PSCA-positive tumor by successive immunoPET/fluorescence, which can potentially be translated for preoperative whole-body prostate cancer detection and intraoperative surgical guidance in patients.

Key words: immunoPET, fluorescence, prostate cancer, antibody fragment, molecular imaging

Introduction

Despite recent advances in prostate cancer treatment, definitive diagnosis requires taking biopsy cores, and there is a critical demand for improved disease detection, staging and stratification. Noninvasive imaging methods, including ultrasound, magnetic resonance imaging (MRI), positron emission tomography (PET), and single-photon emission computed tomography (SPECT), have been adapted

to aid prostate cancer diagnosis, yet each has its limitations [1, 2]. For example, ^{99m}Tc-methylene diphosphonate bone scintigraphy is widely used to detect bone metastases, but it is not specific for prostate cancer [2]. MRI is a highly sensitive and reliable strategy for local staging and identification of soft tissue lesions, but may not be sensitive enough to detect lymph node metastases or differentiate from inflammation [1]. Additional challenges occur during surgery, where difficulty visualizing positive margins, including extracapsular extensions and lymph node metastases, can increase the probability of incomplete resection and therefore tumor recurrence [3, 4]. Wide-resection strategies can damage surrounding tissues such as rectum, urinary sphincter, and erectile nerves, which can lead to urinary incontinence and impotence [5]. The transition to robot-assisted radical prostatectomy has improved oncological, continence, and potency outcomes [6], and this surgical advancement can be complemented with disease-specific optical imaging agents for further improvement in patient outcome. An effective imaging agent can provide a preoperative whole-body image by PET, and intraoperatively identify tumor margins by fluorescence to improve surgical outcome.

Molecular imaging of prostate cancer by PET has been successful in identifying primary and metastatic disease, and it is a powerful tool to guide therapy selection, stratify patients, and monitor response to treatment. The most commonly used PET tracer, 2-deoxy-2-[^{18}F]fluoro-D-glucose (^{18}F-FDG), had limited success in differentiating primary prostate carcinoma from hyperplasia due to the low metabolism of prostate cancer, and therefore other PET tracers have emerged. ^{11}C-choline, ^{18}F-fluorocholine, and ^{11}C-acetate are used to image lipogenesis in prostate cancer, while the recently approved ^{18}F-fluociclovine (FACBC) targets amino acid transport systems [7]. These processes are upregulated in prostate cancer, but they can also occur in benign tissues. Therefore, antibodies, antibody fragments, and peptides based on targeting prostate cancer biomarkers such as prostate-specific membrane antigen (PSMA) [8, 9] and gastrin-releasing peptide receptor (GRPR) [2, 10], have also been developed for PET imaging as well as therapy.

A promising target for imaging and therapy is Prostate Stem Cell Antigen (PSCA), a cell-surface marker upregulated in the majority of prostate cancers and metastases, as well as pancreatic, bladder, and stomach cancer [11]. Increased expression of PSCA correlates with more severe tumor stage, Gleason score, and progression towards androgen independence [12, 13], and pre-clinical molecular imaging has previously been used to detect PSCA-positive prostate [14-16] and pancreatic cancer [17]. As a cell-surface marker, PSCA is a promising target for prostate cancer imaging due to overexpression in primary prostate cancer (88-94%), bone metastases (87-100%), as well as lymph nodes and liver metastases (67%). PSCA can be targeted by immunoPET, which combines the high specificity of antibodies with the sensitivity of PET.

Engineered antibody fragments, such as the minibody (scFv-C_H3 dimer, 80 kDa), clear more quickly compared to full-length antibodies for high tumor-to-background images at short imaging times (next day for the minibody) [18]. The serum half-life ($t_{1/2}$) of the minibody (5-6 h in mice) pairs well with longer-lived radionuclides, including positron-emitting iodine-124 (^{124}I, $t_{1/2}$ = 4.2 days) and zirconium-89 (^{89}Zr, $t_{1/2}$ = 3.3 days), both of which also have been successfully used in the clinic [18]. Tumor uptake of ^{124}I and ^{89}Zr-minibodies peaks around 8 h post injection (p.i.), and unbound tracer is sufficiently cleared by 20 h p.i. to enable imaging in mice.

The humanized parental anti-PSCA A11 minibody (Mb) was previously radiolabeled for high-contrast immunoPET of PSCA-expressing prostate cancers [14]. Both ^{124}I-A11 Mb and ^{89}Zr-A11 Mb successfully targeted transduced (22Rv1-PSCA) and endogenous (LAPC-9) PSCA-expressing prostate cancer xenografts, and ^{124}I-A11 Mb resulted in higher tumor-to-tissue contrast images. Additionally, ^{124}I-A11 Mb was successfully used to monitor PSCA downregulation in LAPC-9 xenografts in response to enzalutamide treatment [15]. Therefore, we propose that A11 Mb can be modified and successfully employed for dual-modality PET imaging and fluorescence imaging.

Near-infrared fluorescence (NIRF) imaging-guided surgery has emerged as a tool to visualize tumor margins for improved resection [19, 20]. NIRF dyes (traditional window 700-900 nm, recently extended to 1,700 nm [21]) allow for light penetration at a greater depth (millimeters) than fluorophores in the visible light range (micrometers) [20], as well as decreased background fluorescence and scattering. NIR fluorophores used to conjugate to target-specific probes include IRDye800CW (available clinical grade), indocyanine green (ICG), and the cyanines Cy5, Cy5.5, or Cy7, which are more easily detected in a preclinical setting [20, 22]. For example, anti-prostate-specific membrane antigen (PSMA) antibody J591-ICG was used to successfully detect PSMA-positive tumors [23], and anti-PSMA antibody and antibody fragments-IR700 were evaluated as photoimmunotherapy agents [24]. PSCA has also been targeted for FIGS of prostate cancer in a study

using Cy5-labeled anti-PSCA A2 cys-diabody (A2 cDb) to detect tumors implanted intramuscularly to mimic invasive growth [25].

A dual-labeled molecule ensures that the radioactive and optical signals are carried on the same molecule, and therefore targeting and imaging will be consistent. Dual-labeled antibodies and peptides for SPECT/fluorescence and PET/fluorescence have been evaluated in several preclinical models [26] including PSMA-positive prostate cancer [27-30]. Indium-111-DOTA-girentuximab-IRDye800CW was successfully used in a recent clinical trial for preoperative and intraoperative guidance in renal cell carcinoma patients [31]. We propose that engineered antibody fragments are highly suited for dual-labeling without perturbation of their kinetics and targeting, and offer next-day high contrast immunoPET and fluorescence images. A recent study successfully used a dual-labeled antibody fragment, ^{124}I-A2 cDb-IRDye800CW, for same-day immuno-PET/fluorescence to detect PSCA-positive patient-derived pancreatic cancer xenografts [32]. Therefore, dual immunoPET/fluorescence imaging with an anti-PSCA antibody fragment could be used to detect PSCA-positive prostate cancer.

In the present study, a cysteine-modified humanized anti-PSCA A11 Mb (A11 cMb) was developed and dually labeled for successive immunoPET/fluorescence imaging. The efficacy was demonstrated in two subcutaneous models and one orthotopic prostate cancer model, and dual-labeled A11 cMb was successfully used to detect PSCA-positive tumors with both imaging modalities.

Methods

Protein production and characterization

Details of protein cloning, expression, and purification, and cell binding assays can be found in the supplemental methods.

Cell lines and tumor models

Details on cell lines and tumor models can be found in the supplemental methods. Briefly, the 22Rv1 human prostate cell line (ATCC CRL-2505) was previously transduced with retrovirus to express PSCA (22Rv1-PSCA) [33]. The PC3 human prostate cell line (ATCC CRL-1435) was previously transfected to express PSCA [33] and FLuc to produce the PC3-PSCA-FLuc cell line. Tumors were established in 8- to 10-week-old male nu/nu mice (*Foxn1^{nu}*, Jackson Laboratories). Bilateral s.c. tumors were implanted using 22Rv1 and 22Rv1-PSCA cells, or PC3 and PC3-PSCA-FLuc cells (0.5-1×10^6), and allowed to grow to 100-200 mm^3 before imaging (measured bilaterally). 22Rv1-PSCA-FLuc cells (5×10^3) were implanted orthotopically, and the tumors were measured to be 1.8 ± 0.6 g at time of sacrifice. Protocols for all animal studies were approved by the UCLA Animal Research Committee.

Site-specific mal-Cy5.5 conjugation

A11 cMb was site-specifically labeled with maleimide-Cy5.5 (mal-Cy5.5) by selective reduction of and conjugation to C-terminal cysteines. In a typical reaction, 200 µg of protein at 1 mg/mL in phosphate-buffered saline (PBS) was reduced using a 2-fold molar excess of tris(2-carboxyethyl)phosphine (TCEP, Pierce) for 30 min at room temperature. Equimolar mal-Cy5.5 (Amersham, GE Healthcare) was added to the reduced A11 cMb for 2 h at room temperature. Excess mal-Cy5.5 was removed using a Micro Bio-Spin™ Size Exclusion Columns (Bio-Rad) pre-equilibrated with PBS. Dye-to-protein ratio (D:P) was determined by measuring the protein (280 nm) and Cy5.5 absorbance (675 nm) with a spectrophotometer (NanoDrop 2000). Successful conjugation was confirmed by sodium dodecyl sulfate polyacrylamide gel electrophoresis (SDS-PAGE) and size exclusion chromatography (SEC).

For SEC, a Superdex 200 10/30 GL column (GE Healthcare) was used with an ÄKTA purifier (GE Healthcare) with PBS as the mobile phase (0.5 mL/min). Absorbance at 280 nm (protein) and 675 nm (Cy5.5) was recorded. The following protein standards were used: beta-amylase (200 kDa), bovine serum albumin (66 kDa), and carbonic anhydrase (29 kDa) (Sigma).

SCN-DFO conjugation

A11 cMb was conjugated with the metal chelator p-isothiocyanatobenzyl-deferoxamine (p-SCN-Bn-DFO, B-705, Macrocyclics) for ^{89}Zr-radiolabeling [34]. In a typical reaction, 3-fold molar excess p-SCN-Bn-DFO was added to A11 cMb or A11 cMb-Cy5.5, and the reaction was immediately adjusted to pH 9 using 0.1 M sodium bicarbonate (1/10 volume). The reaction was allowed to proceed for 30 min at 37 °C, and excess SCN-DFO was removed by size exclusion spin column.

Cell binding (flow cytometry)

The apparent affinity of A11 cMb was determined by flow cytometry using 22Rv1-PSCA and 22Rv1 control cells, or PC3-PSCA and PC3 control cells. A11 cMb and A11 cMb-Cy5.5 were each incubated with 100,000 cells at concentrations varying from 0-1 µM (2 h on ice, triplicate). Samples were washed three times with PBS + 1% FBS + 0.02% sodium azide. Goat anti-human IgG-Dylight 649 (Jackson ImmunoResearch Laboratory, Inc.) was the

secondary antibody used to detect bound A11 cMb as previously described [14]. Samples were run on the BD-LSRFortessa X-20 analyzer and the results were analyzed using FlowJo (v9.3.2) to determine mean fluorescence intensity of the cells. GraphPad Prism 7.0a was used to fit the data using the one site saturation binding model.

Radiolabeling with ^{89}Zr and ^{124}I

^{89}Zr-oxalate (3D Imaging LLC) in 1 M oxalic acid was buffered in 2 M Na_2CO_3 (0.4× volume of ^{89}Zr) and 1 M HEPES pH 7.2-7.5 (2.5× volume of ^{89}Zr) [34]. In a typical reaction, ^{89}Zr-A11 cMb-Cy5.5 was prepared by incubating 100 µg of 1 mg/mL DFO-A11 cMb-Cy5.5 with 0.5 mCi (18.5 MBq) ^{89}Zr at pH 7 for 1 h at room temperature.

^{124}I-A11 cMb, and ^{124}I-A11 cMb-Cy5.5 were prepared using pre-coated Iodogen tubes according to the manufacturer's instructions (Pierce). In a typical reaction, 100 µg of 1 mg/mL A11 cMb or A11 cMb-Cy5.5 was incubated with 0.5 mCi (18.5 MBq) Na-^{124}I (3D Imaging LLC) in 0.1 M Tris, pH 8.0 for 10 min at room temperature.

Radiolabeled proteins were purified by size exclusion spin columns pre-equilibrated with 1% fetal bovine serum (FBS)/PBS. Radiolabeling efficiency and radiochemical purity were assessed by Instant Thin Layer Chromatography (ITLC strips for radiolabeled antibodies, Biodex Medical System) with 20 mM citrate pH 5.0 as the solvent for ^{89}Zr-labeled proteins and saline (0.9% sodium chloride) as the solvent for radioiodinated proteins. The strips were analyzed by gamma counting (Wizard 3" 1480 Automatic Gamma Counter, Perkin-Elmer).

The immunoreactive fraction was determined by the Lindmo method (1-50×10^6 cells) [35]. Radiolabeled A11 cMb (0.9-1.8 ng) was incubated with excess antigen using 22Rv1-PSCA (50×10^6 cells) or PC3-PSCA (50×10^6 cells) in 0.5 mL 1% FBS/PBS in triplicate for 1 h at room temperature. 22Rv1 or PC3 cells were used as a negative control. Cells were centrifuged and washed twice in 1% FBS/PBS, and the cell pellet and supernatant were assessed using a gamma counter.

MicroPET/CT imaging

Mice were administered Lugol's potassium iodide solution (Sigma-Aldrich) and potassium perchlorate (Sigma-Aldrich) to block nonspecific thyroid and stomach uptake, respectively [36, 37]. ^{124}I-A11 cMb (n=3, bilateral 22Rv1 and 22Rv1-PSCA s.c.), ^{124}I-A11 cMb-Cy5.5 (n=3, bilateral 22Rv1 and 22Rv1-PSCA s.c.; n=5, bilateral PC3 and PC3-PSCA s.c.), or ^{89}Zr A11 cMb-Cy5.5 (n=5, orthotopic 22R1-PSCA) (20-90 µCi, 0.74-3.33 MBq, 10-20 µg) in 0.1 mL saline was injected via tail vein. Immediately after injection or at 22 h p.i., mice were anesthetized with 1.5% isoflurane and 10-min static scans were acquired using an Inveon microPET scanner (Siemens), followed by 1-min microCT scans (CrumpCAT [38]). Following the final imaging time point, blood and organs were collected, weighed, and gamma-counted for *ex vivo* biodistribution. Uptake was calculated as % injected dose per gram of tissue (%ID/g) based on a standard containing 1% of the ID.

Dual PET/optical imaging

Following microPET/CT scans, post-mortem NIRF imaging was completed with the skin removed in the IVIS Lumina II (Perkin Elmer) using the following settings: emission = Cy5.5, excitation = 675 nm, 1 s exposure. The tumors and organs were excised and imaged *ex vivo* to compare relative fluorescence signals without obstruction by other organs.

Data analysis

MicroPET images were reconstructed by ordered subset expectation maximization-maximum a posteriori (OSEM-MAP, Inveon Acquisition Workplace). Images were analyzed and displayed using AMIDE [39]. MicroPET/CT overlays are displayed as maximum intensity projections (MIP) of the whole-body or 0.2 mm transverse slices. Fluorescence images were analyzed using the Living Image software (Perkin Elmer). Biodistribution graphs are depicted as scatter plots (with median and range) using GraphPad Prism (version 7.0a for Mac OS X, GraphPad Software). Statistical analysis was performed using multiple Student's *t*-tests, $P<0.05$, and p-values were corrected using the Holm-Šídák method. All values in the tables are reported as mean ± SD.

Results

Biochemical characterization of A11 cMb and conjugated derivatives

Purity and correct assembly of the A11 cMb (scFv-C_H3 dimer) and A11 cMb site-specifically conjugated with the near-infrared dye mal-Cy5.5 (**Figure 1**) was confirmed by SDS-PAGE analysis and size exclusion chromatography (SEC) (**Figure 2** and **Figure S1A-B**). A11 cMb and A11 cMb-Cy5.5 migrated as a single band approximately at the molecular weight calculated from the sequence (80.02 kDa) (**Figure S1A-B**). The size of the A11 cMb was estimated to be 70 kDa from interpolation of the SEC elution profile with known SEC standards (**Figure S1C**). A11 cMb-Cy5.5 and dual-labeled DFO-A11 cMb-Cy5.5 eluted as single peaks (27.07 min and 27.01 min, respectively) similar to the unconjugated A11 cMb, confirming that dimeric minibody conformation was not impaired (**Figure 2A**). Similar elution profiles

of the absorbance at 280 nm (protein) and 675 nm (Cy5.5) demonstrated the fluorophore was associated with the protein (**Figure 2A**). A mean hydrodynamic diameter of 7.5 nm for A11 cMb was determined by dynamic light scattering (**Figure S1D**).

Mass spectrometry confirmed modification with Cy5.5 was specific to the C-terminal cysteine leaving the hinge unmodified (**Figure S1E**). Preliminary imaging studies (data not shown) with a higher D:P of 2:1 showed altered pharmacokinetics and biodistribution with higher uptake in the liver. Therefore, the optimized dye-to-protein (D:P) molar ratio of 0.6-0.8:1 was used to minimize impact on the biodistribution.

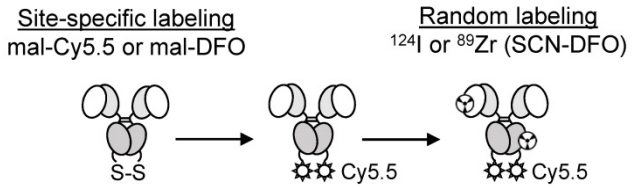

Figure 1. Schematic of the dual-labeled A11 cMb. Site-specific labeling to the A11 cMb C-terminal cysteines (reduced with TCEP) by maleimide-thiol chemistry. For radiolabeling, ^{124}I and SCN-DFO (chelates ^{89}Zr) are randomly labeled to surface-exposed tyrosine or lysine residues, respectively.

A11 cMb-Cy5.5 retains low nanomolar affinity binding to PSCA$^+$ cells

Flow cytometry analysis showed strong binding of A11 cMb-Cy5.5 to PSCA-expressing cells (22Rv1-PSCA). The selectivity for PSCA was confirmed using PSCA-negative cells (22Rv1) (**Figure 2B**). The apparent affinity (K_D value) calculated from saturation binding curves for A11 cMb-Cy5.5 (16.7 ± 3.4 nM, n=4, **Figure 2C**) was comparable to that of the parental A11 Mb (13.7 ± 1.4 nM, [15]). This was also similar to the apparent affinities of A11 cMb-Cy5.5 (22.7 ± 2.7 nM, n=7) and dual-labeled DFO-A11 cMb-Cy5.5 (26.8 ± 2.3 nM, n=3) to PC3-PSCA cells (data not shown) (P>0.05 for all).

ImmunoPET and fluorescence imaging of subcutaneous 22Rv1-PSCA tumors using single-labeled ^{124}I-A11 cMb and dual-labeled ^{124}I-A11 cMb-Cy5.5

^{124}I-A11 cMb and ^{124}I-A11 cMb-Cy5.5 had specific activities of 1.0-3.9 μCi/μg (37-144 kBq/μg) and 0.6-5.9 μCi/μg (22-219 kBq/μg), respectively, and both probes retained high immunoreactivity to PSCA-positive cells (>70%) (**Table 1**). For the 22Rv1-PSCA s.c. model, 20 μg of ^{124}I-A11 cMb or ^{124}I-A11 cMb-Cy5.5 with a final D:P of 0.7:1 was injected into nude mice. High-contrast immunoPET images acquired 22 h p.i. showed specific uptake of ^{124}I-A11 cMb or ^{124}I-A11 cMb-Cy5.5 in the 22Rv1-PSCA tumors compared to minimal uptake in the antigen-negative 22Rv1 tumors, blood, and background tissues (**Figure 3A-B**).

Specific uptake in the PSCA-positive tumors was confirmed by *ex vivo* biodistribution at 22 h p.i., with similar values for both ^{124}I-A11 cMb-Cy5.5 (12 ± 1.3 %ID/g) and ^{124}I-A11 cMb (12 ± 4.2 %ID/g, P>0.05) (**Figure 3C** and **Table 2**). Antigen-specific uptake in 22Rv1-PSCA tumors was significantly higher than nonspecific uptake in 22Rv1 tumors, resulting in positive-to-negative tumor ratios of 13:1 and 8:1, for ^{124}I-A11 cMb-Cy5.5 and ^{124}I-A11 cMb, respectively (**Table 2**). Importantly, no significant difference in uptake, clearance, and biodistribution between the single (^{124}I-A11 cMb) and the dual-modality (^{124}I-A11 cMb-Cy5.5) tracer was observed (**Figure 3C** and **Table 2**).

Table 1. Radiolabeling and immunoreactivity.

	^{124}I-A11 cMb	^{124}I-A11 cMb-Cy5.5	^{89}Zr-A11 cMb-Cy5.5
Radiolabeling Efficiency	81 ± 21% n=3	69 ± 23% n=6	99 ± 1% n=3
Radiochemical Purity	99.1 ± 0.6% n=3	99.1 ± 0.90% n=6	99.7 ± 0.1% n=2
Specific Activity	2.5 ± 1.5 μCi/μg n=3	3.3 ± 2.1 μCi/μg n=6	5.8 ± 0.7 μCi/μg n=3
Immunoreactive Fraction (r) for 22Rv1-PSCA	>0.76 n=3	>0.76 n=4	0.77 n=1
Immunoreactive Fraction (r) for PC3-PSCA	n/a	0.82 n=1	0.80 n=1

Values are reported as mean ± standard deviation (SD)

Table 2. Mice bearing 22Rv1-PSCA and 22Rv1 xenografts show similar *ex vivo* biodistribution of ^{124}I-A11 cMb or ^{124}I-A11 cMb-Cy5.5 at 22 h post-injection (P=n.s. for all tissues).

	^{124}I-A11 cMb %ID/g ± SD	^{124}I-A11 cMb-Cy5.5 %ID/g ± SD
22Rv1-PSCA	12 ± 4.2	12 ± 1.3
22Rv1	1.7 ± 1.0	1.2 ± 0.6
Blood	3.3 ± 0.1	1.9 ± 0.5
Heart	1.2 ± 0.1	0.7 ± 0.3
Lung	1.7 ± 0.1	1.2 ± 0.1
Liver	0.6 ± 0.0	0.9 ± 0.1
Kidney	1.1 ± 0.0	1.0 ± 0.1
Spleen	0.7 ± 0.1	0.5 ± 0.1
Stomach	2.1 ± 0.3	1.3 ± 0.0
Intestine	0.4 ± 0.0	0.2 ± 0.1
Muscle	0.2 ± 0.0	0.1 ± 0.0
Pos:Neg Tumor	8.1 ± 2.8	13 ± 7.7
Pos Tum:Blood	3.7 ± 1.2	6.6 ± 1.9
Neg Tum:Blood	0.5 ± 0.3	0.6 ± 0.2
Pos Tum:Muscle	54 ± 20 n=3	130 ± 39 n=3

%ID/g: % injected dose per gram; tum: tumor.
Values are reported as mean ± SD.

Post-mortem fluorescence imaging was completed with the skin removed in order to mimic an intraoperative setting. In mice injected with ^{124}I-A11 cMb-Cy5.5, strong fluorescence signal was detected in

the 22Rv1-PSCA tumors with minimal background signal in 22Rv1 tumors and surrounding muscle (**Figure 3D**). *Ex vivo* optical imaging of the resected tumors allowed comparison of relative fluorescence signals without obstruction by other organs. Consistent with the *in situ* results, high fluorescence signal was seen in the 22Rv1-PSCA tumors compared to 22Rv1 tumors (**Figure 3E**).

ImmunoPET and fluorescence imaging of subcutaneous PC3-PSCA tumors using ^{124}I-A11 cMb-Cy5.5

A subcutaneous PC3-PSCA tumor model was used to test the feasibility of imaging moderate levels of PSCA (5.2 ± 2.6×10^5 antigens/cell). MicroPET/CT of nude mice (n=5) bearing PC3-PSCA and control PC3 tumors showed high uptake of ^{124}I-A11 cMb-Cy5.5 in positive tumors at 22 h p.i. Nonspecific uptake in the stomach and thyroid is visible in images set at a scale of 0.2-2 %ID/g (**Figure 4A**), as these organs scavenge free iodine and were likely incompletely blocked. The *ex vivo* biodistribution confirms the imaging results with significantly higher uptake in PC3-PSCA tumors (2.9 ± 0.6 %ID/g) compared to PC3 tumors (0.7 ± 0.4 %ID/g) (*P*=0.0002), resulting in a positive-to-negative tumor ratio of 5.6:1, and PC3-PSCA tumor-to-muscle ratio of 54:1 (**Figure 4B** and **Table 3**).

Ex vivo optical imaging allowed comparison between the PC3-PSCA tumors, which were detected by Cy5.5 fluorescence, and PC3 control tumors, which had little to no fluorescence signal (**Figure 4C**). *Ex vivo* analysis showed expected autofluorescence (stomach, intestines) and additional signal in liver, kidneys, and bladder due to tracer clearance (**Figure S2**).

ImmunoPET and fluorescence imaging of intraprostatic 22Rv1-PSCA tumors using ^{89}Zr-A11 cMb-Cy5.5

In order to test dual-imaging at the natural site of prostate disease, an orthotopic model was assessed. These studies were conducted using ^{89}Zr because signal from ^{124}I clearance to the bladder interfered with visualization of activity accumulated in the prostate (data not shown). Mice were intraprostatically implanted with 22Rv1-PSCA-Fluc-GFP cells, and tumors grew extensively with significant bioluminescence signal (n=4) or low signal (n=1), which was designated "limited disease" (**Figure S3**).

^{89}Zr-A11 cMb-Cy5.5 immunoPET at 22 h p.i. showed specific uptake in the prostate tumors with extensive disease compared to minimal prostate signal in the mouse with limited disease (**Figure 5A**). *Ex vivo* biodistribution at (22 h p.i.) confirmed specific uptake in the 22Rv1-PSCA tumors (3.1 ± 0.5 %ID/g), and the tumor-to-blood ratio was quantified to be 3:1. Due to the residualizing nature of the radiometal, activity in organs of clearance was retained at high levels compared with the iodinated A11 cMb (liver: 18 ± 2.7 %ID/g, kidneys: 12 ± 1.2 %ID/g, spleen: 5.1 ± 2.1 %ID/g) (**Figure 5A-B** and **Table 4**). Nonspecific uptake in the bone is due to accumulation of free ^{89}Zr. Importantly, the prostate tumor was clearly distinguished by post-mortem fluorescence imaging compared to adjacent seminal vesicles and bladder, which supports the feasibility of fluorescence guidance for prostate cancer surgery (**Figure 5C**). PSCA-positive tumor growth in the prostate and absence of neoplastic tissue in the surrounding seminal vesicles was confirmed by H&E and anti-PSCA immunohistochemistry (IHC) (**Figure 5D**).

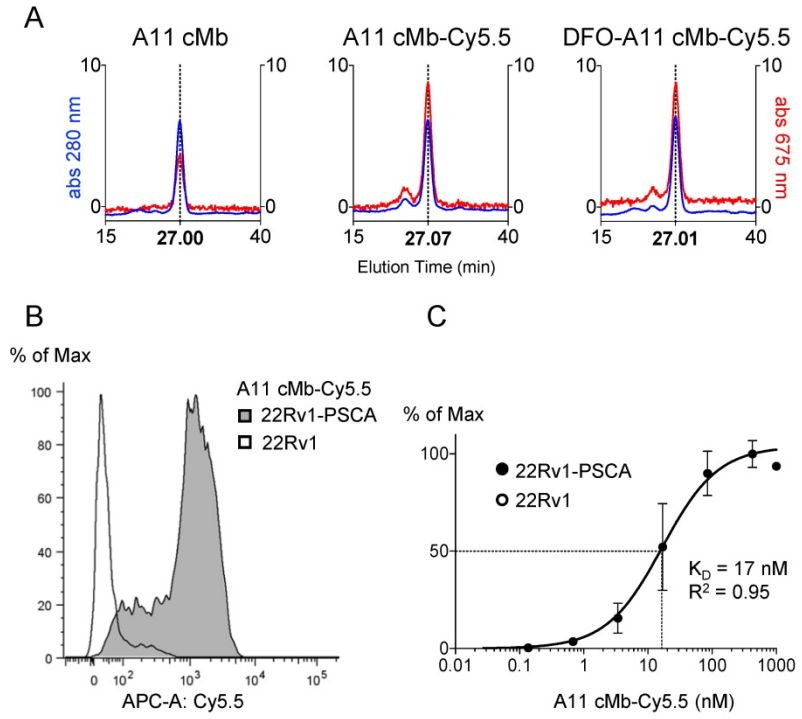

Figure 2. Biochemical characterization of A11 cMb-Cy5.5. (A) Size exclusion chromatography (SEC) elution profiles show A11 cMb, A11 cMb-Cy5.5, and DFO-A11 cMb-Cy5.5 elute in a single peak (27.00 min, 27.07 min, and 27.01 min, respectively), demonstrating the conjugations did not disrupt the minibody dimeric conformation (protein at 280 nm, Cy5.5 at 675 nm). Absorption at 675 nm (Cy5.5) is higher for the conjugated A11 cMb samples. **(B)** Flow cytometry analysis shows A11 cMb-Cy5.5 binding specifically to 22Rv1-PSCA cells. No binding to control 22Rv1 cells was detected. **(C)** Saturation binding study of A11 cMb-Cy5.5 (22Rv1-PSCA and 22Rv1 cells) was used to calculate the half-maximal binding K_D using a one-site specific binding model (n=3, GraphPad).

Table 3. *Ex vivo* biodistribution of ^{124}I-A11 cMb-Cy5.5 in mice bearing PC3-PSCA and PC3 xenografts at 22 h post-injection.

	^{124}I-A11 cMb-Cy5.5
	%ID/g ± SD
PC3-PSCA	2.9 ± 0.6
PC3	0.7 ± 0.4
Blood	1.2 ± 0.2
Heart	0.4 ± 0.2
Lung	0.6 ± 0.3
Liver	0.4 ± 0.1
Kidney	0.5 ± 0.1
Spleen	0.4 ± 0.2
Stomach	3.1 ± 0.6
Intestine	0.2 ± 0.1
Bone	0.2 ± 0.1
Muscle	0.1 ± 0.0
Pros, s.v., b	0.8 ± 0.3
Testes	0.3 ± 0.1
Pos:Neg Tumor	5.6 ± 2.9
Pos Tum:Blood	2.6 ± 0.8
Neg Tum:Blood	0.6 ± 0.3
Pos Tum:Muscle	54 ± 21
	n=5

%ID/g: % injected dose per gram; b: bladder; pros: prostate; s.v.: seminal vesicles; tum: tumor.
Values are reported as mean ± SD.

Table 4. *Ex vivo* biodistribution of ^{89}Zr-A11 cMb-Cy5.5 in mice bearing intraprostatic 22Rv1-PSCA tumors at 22 h post-injection.

	^{89}Zr-A11 cMb-Cy5.5
	%ID/g ± SD
Prostate Tumor	3.1 ± 0.5
Blood	0.9 ± 0.1
Heart	2.6 ± 0.7
Lung	2.4 ± 1.6
Liver	18 ± 2.7
Kidney	12 ± 1.2
Spleen	5.1 ± 2.1
Stomach	1.1 ± 0.2
Intestine	2.6 ± 0.3
Bone	4.4 ± 2.3
Muscle	0.4 ± 0.1
Testes	2.9 ± 1.4
Pros Tum:Blood	3.4 ± 0.2
Pros Tum:Muscle	7.7 ± 1.0
	n=4, except blood n=3

%ID/g: % injected dose per gram; pros: prostate; tum: tumor.
Values are reported as mean ± SD.

Discussion

Primary prostate cancer and regional lymph node metastases can be treated by surgical resection. However, patients often suffer from over and under-treatment due to inaccurate diagnosis or inability to visualize positive margins during surgery. Dual-modality PET/fluorescence imaging could provide non-invasive whole-body disease detection and intraoperative fluorescence guidance, and therefore improve prostate cancer treatment.

In this study, the anti-PSCA antibody fragment A11 cys-minibody (A11 cMb) was used to generate a novel dual-modality imaging probe. A11 cMb was conjugated with the near-infrared dye Cy5.5 and radiolabeled with either ^{124}I or ^{89}Zr (^{124}I-A11 cMb-Cy5.5 and ^{89}Zr-A11 cMb-Cy5.5). Both tracers showed specific targeting to PSCA-expressing prostate cancer *in vivo* resulting in whole body immunoPET scans visualizing the tumors and fluorescence imaging distinguishing PSCA-positive cancer from surrounding healthy tissue.

Fluorescent modification of A11 cMb did not impair its affinity or specificity of antigen binding. Studies have shown that binding affinity can be affected by conjugation of large hydrophobic moieties, such as near-infrared dyes [40]. Therefore, the Cy5.5 conjugation was directed to the engineered C-terminal cysteine away from the antigen binding sites. A11 cMb-Cy5.5 and DFO-A11 cMb-Cy5.5 specifically bound to PSCA-positive cells with high affinity, similar to previously published unconjugated parental A11 Mb [14] (**Figure 2**). Dual-labeled ^{124}I-A11 cMb-Cy5.5 and ^{89}Zr-A11 cMb-Cy5.5 retained high immunoreactivity for PSCA-positive cells similar to ^{124}I-A11 cMb (**Table 1**), demonstrating that dual-labeling did not impair binding. Fluorophore conjugation can also affect the pharmacokinetics and biodistribution of antibodies and small ligands [20, 28], typically in the form of enhanced liver uptake and faster blood clearance. ^{124}I-A11 cMb-Cy5.5 with a dye-to-protein ratio (D:P) of 0.7-0.8:1 demonstrated similar tumor uptake and minimal changes in biodistribution compared with ^{124}I-A11 cMb.

Fluorescence imaging-guided surgery has been shown to improve tumor resection in preclinical studies and several agents have entered clinical trials [41]. Furthermore, dual-modality imaging is increasingly studied in both preclinical and clinical studies [26, 31, 32]. Imaging with a dual-labeled antibody ensures similar biodistribution in both modalities and facilitates clinical translation by avoiding separate testing of distinct imaging tracers. While immunoPET provides whole-body, quantitative information with unlimited depth, it suffers from low resolution and time constraints due to radioactive decay. NIRF fluorophores, on the other hand, show low depth of penetration [42] but excellent cell-level resolution. Unlike the radiolabel, the fluorophore does not have a physical half-life (cellular half-life = 3.9 days [43]) and therefore allows longer detection of the signal for surgical guidance.

PSCA is expressed in virtually all prostate cancers (83-100%) as well as in prostate cancer metastases to bone and lymph nodes [11, 13, 44, 45]. However, a wide range of PSCA expression levels, correlating with progression and prognosis, was found by quantitative reverse transcriptase-PCR analysis of clinical prostate metastases specimens [44]. Because increased PSCA corresponds with increased Gleason score and clinical stage, we therefore

evaluated the dual-modality A11 cMb in two s.c. models with different levels of PSCA expression: 22Rv1-PSCA (high-PSCA) and PC3-PSCA (moderate PSCA). Importantly, ^{124}I-A11 cMb-Cy5.5 immuno-PET/fluorescence imaging resulted in high-contrast PET and fluorescence images in both high- and moderate PSCA-positive prostate cancer models. Although antigen expression does not necessarily correlate with tumor uptake, as other factors such as tumor vasculature can affect accessibility, the dual-modality A11 cMb could facilitate detection in different stages of prostate cancer.

The longer-lived radionuclides ^{124}I and ^{89}Zr are most commonly used for labeling antibodies, and in this study, we compared specific tumor uptake and contrast to normal tissue of both ^{124}I- and ^{89}Zr-labeled A11 cMb-Cy5.5 in preclinical prostate cancer models. ^{124}I and ^{89}Zr differ regarding their physical properties, protein conjugation chemistry, and biological metabolism, which can lead to significant differences in uptake and retention of the radioactive signal. ^{124}I is a nonresidualizing radiolabel when radioiodinated using standard methods such as Iodogen. Upon internalization and degradation of such radioiodinated proteins, metabolites including iodotyrosine are not retained by the cell, leading to low background and thereby high contrast. These characteristics are advantageous when imaging targets retained on the cell surface, like PSCA that has previously been shown to internalize slowly [14]. Concordantly, immunoPET studies using ^{124}I-labeled parental A11 Mb [14], ^{124}I-A11 cMb and ^{124}I-A11 cMb-Cy5.5 achieved high-contrast images in the subcutaneous models (22Rv1-PSCA, PC3-PSCA). A previous study using ^{124}I-A11 Mb to image intratibial xenografts supports the hypothesis that the very low background of ^{124}I-A11 cMb-Cy5.5 will be advantageous for targeting bone metastases [15]. In contrast, free ^{89}Zr accumulates in bone and may result in false positives [46].

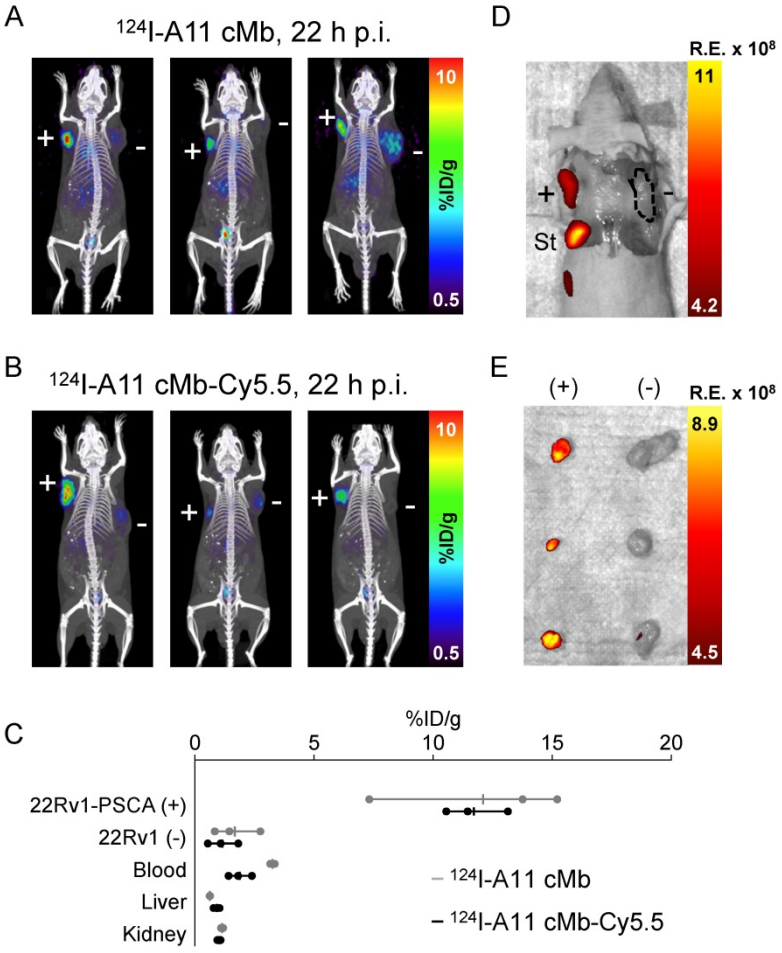

Figure 3. ^{124}I-A11 cMb-Cy5.5 PET/fluorescence shows specific targeting to 22Rv1-PSCA subcutaneous tumors. (A) ^{124}I-A11 cMb and **(B)** ^{124}I-A11 cMb-Cy5.5 PET/CT scans show antigen-specific uptake in 22Rv1-PSCA tumors (+, left shoulder) and minimal nonspecific uptake in 22Rv1 (-, right shoulder) tumors at 22 h post-injection (nude mice, n=3 per group). Images are represented as whole-body maximum intensity projections (MIPs). **(C)** *Ex vivo* biodistribution (22 hours p.i.) confirms high uptake in 22Rv1-PSCA tumors and low activity in all other tissues. The addition of Cy5.5 at a low dye-to-protein ratio did not alter biodistribution. **(D-E)** Post-mortem Cy5.5 fluorescence images show specific signal in PSCA-positive tumors. The signal from the stomach is due to autofluorescence. R.E.: radiance efficiency ($\frac{\text{photons/sec/cm}^2\text{/sr}}{\mu\text{w/cm}^2}$); St: stomach.

A major benefit of imaging with a residualizing radiometal (^{89}Zr) is better signal retention, as ^{89}Zr-radiometabolites get trapped in the cell upon internalization, and higher spatial resolution due to a shorter mean positron range (1.1 mm for ^{89}Zr vs 3.0 mm for ^{124}I). These factors are crucial when imaging small structures like the prostate; hence, ^{89}Zr-A11 cMb-Cy5.5 was used to image orthotopic prostate cancer. A further advantage compared with ^{124}I is that ^{89}Zr is not excreted through urine, assuring minimal interference from activity in the bladder.

^{89}Zr-A11 cMb-Cy5.5 immunoPET/fluorescence imaging of the orthotopic model demonstrated successful visualization and delineation of 22Rv1-PSCA tumors growing at the site of natural disease, which is an important finding as tumor localization and accessibility are known to affect tumor targeting and tracer uptake, and may account for the difference in tumor uptake between the orthotopic and s.c. models. These promising results and the fact that the dual-modality tracer is based on a humanized antibody fragment suggest that ^{89}Zr- and ^{124}I-labeled A11 cMb-Cy5.5 could be clinically translated for imaging and surgical guidance in prostate cancer.

The results from an ongoing Phase I trial evaluating ^{124}I-parental A11 Mb for immunoPET (NCT02092948) will inform on the pharmacokinetics of radiolabeled minibody in patients.

Future studies should include surgical studies to mimic the clinical setting (radical prostatectomy) and confirm a survival benefit of resecting tumors guided by real-time fluorescence imaging. Furthermore, more clinically relevant metastatic prostate cancer models should be imaged to ensure that positive pelvic lymph nodes are detectable both preoperatively using ^{89}Zr-A11 cMb-Cy5.5 immunoPET and intraoperatively using fluorescence, as the current clinical standard using frozen section histology to confirm which lymph nodes to resect is time-intensive [47].

Dual-modality imaging can also be applied to antibodies against other prostate cancer targets. For example, GRPR has been successfully targeted by ^{68}Ga-HZ220-IRDye 650 in mice bearing PC3 xenografts for PET/NIRF imaging [29], as well as by ^{68}Ga-IRDye800CW-BBN in a first-in-human study in patients with glioblastoma [48]. Antibodies and peptides targeting PSMA have been extensively explored for PET [49], and more recently validated for optical imaging [20] and dual SPECT/fluorescence imaging [26-28]. Dual-labeled ^{111}In-PSMA-targeting-urea-IRDye800CW [27] and ^{111}In-anti-PSMA antibody D2B-IRDye800CW [28] successfully detected prostate cancer lesions in mice by SPECT/NIRF, and the anti-PSMA antibody MDX1201-A488 is currently being evaluated for FIGS in patients receiving robot-assisted laparoscopic prostatectomy (NCT02048150). However, PSMA is also expressed in normal tissues, such as the ganglia close to the location of typical lymph node metastases, which could result in false positives, and PSMA overexpression is not present in 10% of patients [50]. Therefore, it would be useful to also explore PSCA as an additional target for prostate cancer diagnosis and therapy.

In summary, specific targeting to human PSCA -positive prostate cancer was achieved by *in vivo* administration of ^{124}I-A11 cMb-Cy5.5 and ^{89}Zr-A11 cMb-Cy5.5 for immunoPET and fluorescence imaging. Dual-modality imaging was successful in s.c. models with high and moderate PSCA expression, demonstrating the ability of the A11 cMb to target a range of antigen expression. In the intraprostatic model, fluorescence clearly distinguished the prostate tumor from surrounding relevant tissues. This work has translational potential for noninvasive preoperative whole-body imaging and additional real-time intraoperative guidance in PSCA-positive prostate cancer.

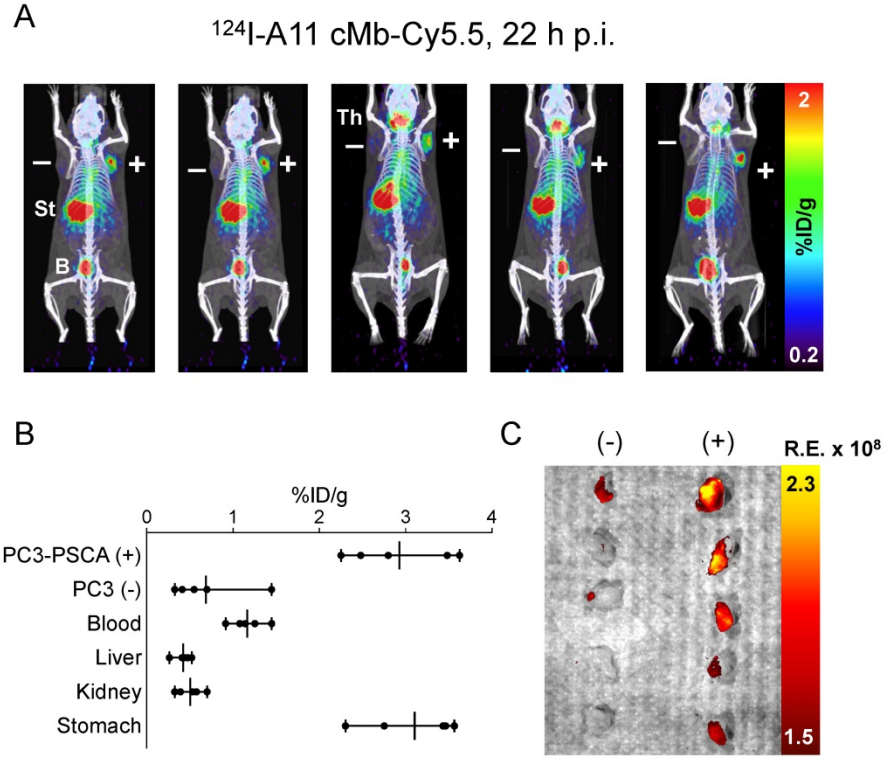

Figure 4. ^{124}I-A11 cMb-Cy5.5 PET/fluorescence shows specific targeting of PC3-PSCA subcutaneous tumors. (A) ^{124}I-A11 cMb-Cy5.5 PET/CT scans at 22 h post-injection (nude mice, n=5) show specific uptake in subcutaneous PC3-PSCA (+, right shoulder) tumors and no nonspecific uptake in PC3 tumors (PSCA-, left shoulder). Images are represented as whole-body MIPs. **(B)** *Ex vivo* biodistribution (22 h p.i.) confirms higher %ID/g uptake in PC3-PSCA tumors than PC3 tumors. **(C)** *Ex vivo* fluorescence (Cy5.5) imaging revealed strong fluorescence signal in PC3-PSCA tumors and excellent contrast to PC3 control tumors. B: bladder; R.E.: radiance efficiency ($\frac{\text{photons/sec/cm}^2\text{/sr}}{\mu\text{w/cm}^2}$); St: stomach; Th: thyroid.

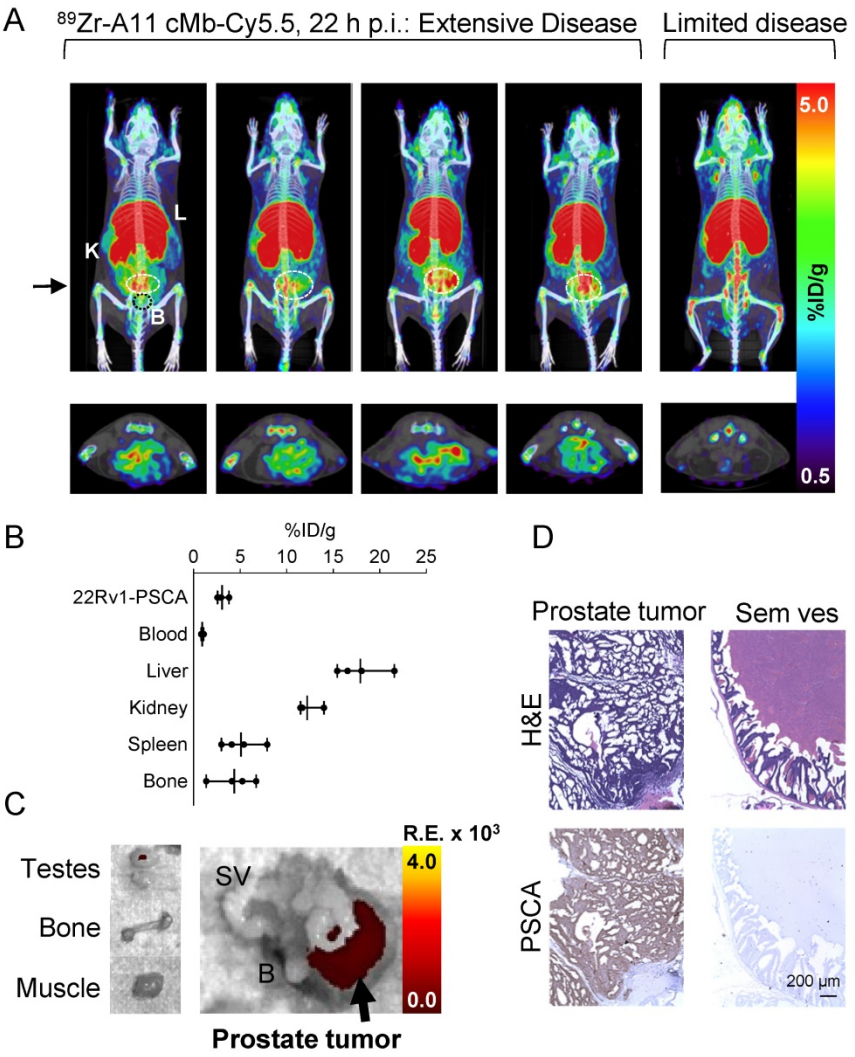

Figure 5. ^{89}Zr-A11 cMb-Cy5.5 targets 22Rv1-PSCA intraprostatic tumors by PET/fluorescence. (A) ^{89}Zr-A11 cMb-Cy5.5 PET/CT at 22 h post-injection of nude mice (n=4) bearing 22Rv1-PSCA-GFP-FLuc intraprostatic orthotopic tumors (outlined by the white dotted circle), compared to a mouse (n=1) with limited disease. The top row images are represented as coronal whole-body MIPs, and the bottom row images are represented as 0.2 mm transverse sections that correspond to the black arrow. The transverse section does not include the bladder (outlined in the left top panel by the black dotted circle). **(B)** *Ex vivo* biodistribution (22 h p.i.) confirms higher %ID/g uptake in 22Rv1-PSCA prostate tumors compared to blood, along with high clearance to the liver and kidney. **(C)** Cy5.5 fluorescence signal is specific to the resected prostate with little to no signal in surrounding seminal vesicles, bladder, or background tissues (testes, bone, and muscle). R.E.: radiance efficiency ($\frac{\text{photons/sec/cm}^2\text{/sr}}{\mu\text{w/cm}^2}$). **(D)** Hematoxylin and eosin (H&E) staining confirms tumor growth in the prostate, which stained positively for PSCA, while surrounding seminal vesicles were negative for PSCA. B: bladder; K: kidney; L: liver; SV: seminal vesicle.

Abbreviations

cMb: cys-minibody; FIGS: fluorescence imaging-guided surgery; IHC: immunohistochemistry; Mb: minibody; MRI: magnetic resonance imaging; NIRF: near-infrared fluorescence; PET: positron emission tomography; PSCA: prostate stem cell antigen; PSMA: prostate specific membrane antigen; SEC: size exclusion chromatography; SPECT: single-photon emission computed tomography.

Supplementary Material

Supplementary figures.
http://www.thno.org/v08p5903s1.pdf

Acknowledgements

The authors thank Felix B Salazar, Amanda C Freise, Kelly Huynh, and Chong Hyun Chang for technical assistance. We thank Waldemar Ladno, Theresa Falls, Olga Sergeeva, Jason Lee, and Arion Chatziioannou from the UCLA Crump Institute Preclinical Imaging Technology Center for assistance with small-animal PET and fluorescence imaging. We thank Roger Moore from City of Hope for completion of mass spectrometry studies, Jeff Calimlim from the Jonsson Comprehensive Cancer Center Flow Cytometry Core for assistance with flow cytometry, and the UCLA Translational Pathology Core Laboratory for histology assistance.

Grant Support

This work was supported by NIH grants R01 CA174294, P30 CA016042, Department of Defense W81 XWH-15-1-0725, and the Dr. Ursula Mandel fellowship. Imaging, flow cytometry, pathology core services were supported by Jonsson Comprehensive Cancer Center (P30 CA016042).

Competing Interests

A. Wu has an ownership interest in, and is a board member and consultant for ImaginAb, Inc.

References

1. Hricak H, Choyke PL, Eberhardt SC, Leibel SA, Scardino PT. Imaging prostate cancer: a multidisciplinary perspective. Radiology. 2007; 243: 28-53.
2. Wibmer AG, Burger IA, Sala E, Hricak H, Weber WA, Vargas HA. Molecular imaging of prostate cancer. Radiographics. 2016; 36: 142-59.
3. Epstein JI, Amin M, Boccon-Gibod L, Egevad L, Humphrey PA, Mikuz G, et al. Prognostic factors and reporting of prostate carcinoma in radical prostatectomy and pelvic lymphadenectomy specimens. Scand J Urol Nephrol Suppl. 2005; 243: 34-63.
4. Yossepowitch O, Briganti A, Eastham JA, Epstein J, Graefen M, Montironi R, et al. Positive surgical margins after radical prostatectomy: a systematic review and contemporary update. Eur Urol. 2014; 65: 303-13.
5. Walsh PC, Marschke P, Ricker D, Burnett AL. Patient-reported urinary continence and sexual function after anatomic radical prostatectomy. Urology. 2000; 55: 58-61.
6. Ficarra V, Novara G, Ahlering TE, Costello A, Eastham JA, Graefen M, et al. Systematic review and meta-analysis of studies reporting potency rates after robot-assisted radical prostatectomy. Eur Urol. 2012; 62: 418-30.
7. Jadvar H. Molecular imaging of prostate cancer with PET. J Nucl Med. 2013; 54: 1685-8.
8. Pandit-Taskar N, O'Donoghue JA, Ruan S, Lyashchenko S, Carrasquillo JA, Heller G, et al. First-in-human imaging with 89Zr-Df-IAB2M anti-PSMA minibody in patients with metastatic prostate cancer: pharmacokinetics, biodistribution, dosimetry, and lesion uptake. J Nucl Med. 2016; 57:1858-1864.
9. Lutje S, Slavik R, Fendler W, Herrmann K, Eiber M. PSMA ligands in prostate cancer - probe optimization and theranostic applications. Methods. 2017; 130: 42-50.
10. Wieser G, Mansi R, Grosu AL, Schultze-Seemann W, Dumont-Walter RA, Meyer PT, et al. Positron emission tomography (PET) imaging of prostate cancer with a gastrin releasing peptide receptor antagonist—from mice to men. Theranostics. 2014; 4: 412-9.
11. Reiter RE, Gu Z, Watabe T, Thomas G, Szigeti K, Davis E, et al. Prostate stem cell antigen: a cell surface marker overexpressed in prostate cancer. Proc Natl Acad Sci U S A. 1998; 95: 1735-40.
12. Han KR, Seligson DB, Liu X, Horvath S, Shintaku PI, Thomas GV, et al. Prostate stem cell antigen expression is associated with gleason score, seminal vesicle invasion and capsular invasion in prostate cancer. J Urol. 2004; 171: 1117-21.
13. Gu Z, Thomas G, Yamashiro J, Shintaku IP, Dorey F, Raitano A, et al. Prostate stem cell antigen (PSCA) expression increases with high gleason score, advanced stage and bone metastasis in prostate cancer. Oncogene. 2000; 19: 1288-96.
14. Knowles SM, Zettlitz KA, Tavare R, Rochefort MM, Salazar FB, Stout DB, et al. Quantitative immunoPET of prostate cancer xenografts with 89Zr- and 124I-labeled anti-PSCA A11 minibody. J Nucl Med. 2014; 55: 452-9.
15. Knowles SM, Tavare R, Zettlitz KA, Rochefort MM, Salazar FB, Jiang ZK, et al. Applications of immunoPET: using 124I-anti-PSCA A11 minibody for imaging disease progression and response to therapy in mouse xenograft models of prostate cancer. Clin Cancer Res. 2014; 20: 6367-78.
16. Wu H, Shi H, Zhang H, Wang X, Yang Y, Yu C, et al. Prostate stem cell antigen antibody-conjugated multiwalled carbon nanotubes for targeted ultrasound imaging and drug delivery. Biomaterials. 2014; 35: 5369-80.
17. Foss CA, Fox JJ, Feldmann G, Maitra A, Iacobuzio-Donohue C, Kern SE, et al. Radiolabeled anti-claudin 4 and anti-prostate stem cell antigen: initial imaging in experimental models of pancreatic cancer. Mol Imaging. 2007; 6: 131-9.
18. Knowles SM, Wu AM. Advances in immuno-positron emission tomography: antibodies for molecular imaging in oncology. J Clin Oncol. 2012; 30: 3884-92.
19. Vahrmeijer AL, Hutteman M, van der Vorst JR, van de Velde CJ, Frangioni JV. Image-guided cancer surgery using near-infrared fluorescence. Nat Rev Clin Oncol. 2013; 10: 507-18.
20. Zhang RR, Schroeder AB, Grudzinski JJ, Rosenthal EL, Warram JM, Pinchuk AN, et al. Beyond the margins: real-time detection of cancer using targeted fluorophores. Nat Rev Clin Oncol. 2017; 14: 347-364.
21. Hong G, Antaris AL, Dai H. Near-infrared fluorophores for biomedical imaging. Nat Biomed Eng. 2017; 1:0010.
22. Nguyen QT, Tsien RY. Fluorescence-guided surgery with live molecular navigation--a new cutting edge. Nat Rev Cancer. 2013; 13: 653-62.
23. Nakajima T, Mitsunaga M, Bander NH, Heston WD, Choyke PL, Kobayashi H. Targeted, activatable, in vivo fluorescence imaging of prostate-specific membrane antigen (PSMA) positive tumors using the quenched humanized J591 antibody-indocyanine green (ICG) conjugate. Bioconjugate Chem. 2011; 22: 1700-5.
24. Watanabe R, Hanaoka H, Sato K, Nagaya T, Harada T, Mitsunaga M, et al. Photoimmunotherapy targeting prostate-specific membrane antigen: are antibody fragments as effective as antibodies? J Nucl Med. 2015; 56: 140-4.
25. Sonn GA, Behesnilian AS, Jiang ZK, Zettlitz KA, Lepin EJ, Bentolila LA, et al. Fluorescent image-guided surgery with an anti-prostate stem cell antigen (PSCA) diabody enables targeted resection of mouse prostate cancer xenografts in real time. Clin Cancer Res. 2016; 22: 1403-12.
26. Lutje S, Rijpkema M, Helfrich W, Oyen WJ, Boerman OC. Targeted radionuclide and fluorescence dual-modality imaging of cancer: preclinical advances and clinical translation. Mol Imaging Biol. 2014; 16: 747-55.
27. Banerjee SR, Pullambhatla M, Byun Y, Nimmagadda S, Foss CA, Green G, et al. Sequential SPECT and optical imaging of experimental models of prostate cancer with a dual modality inhibitor of the prostate-specific membrane antigen. Angew Chem Int Ed Engl. 2011; 50: 9167-70.
28. Lutje S, Rijpkema M, Franssen GM, Fracasso G, Helfrich W, Eek A, et al. Dual-Modality image-guided surgery of prostate cancer with a radiolabeled fluorescent anti-PSMA monoclonal antibody. J Nucl Med. 2014; 55: 995-1001.
29. Zhang H, Desai P, Koike Y, Houghton J, Carlin SD, Tandon N, et al. Dual modality imaging of prostate cancer with a fluorescent and radiogallium-labeled GRP receptor antagonist. J Nucl Med. 2016; 58: 29-35.
30. Hekman MC, Rijpkema M, Bos D, Oosterwijk E, Goldenberg DM, Mulders PF, et al. Detection of micrometastases using SPECT/fluorescence dual-modality imaging in a CEA-expressing tumor model. J Nucl Med. 2017; 58: 706-710.
31. Hekman MC, Rijpkema M, Muselaers CH, Oosterwijk E, Hulsbergen-Van de Kaa CA, Boerman OC, et al. Tumor-targeted dual-modality imaging to improve intraoperative visualization of clear cell renal cell carcinoma: a first in man study. Theranostics. 2018; 8: 2161-70.
32. Zettlitz KA, Tsai WK, Knowles SM, Kobayashi N, Donahue TR, Reiter RE, et al. Dual-modality immunoPET and near-infrared fluorescence (NIRF) imaging of pancreatic cancer using an anti-prostate cancer stem cell antigen (PSCA) cys-diabody. J Nucl Med. 2018; 59: 1398-1405.
33. Saffran DC, Raitano AB, Hubert RS, Witte ON, Reiter RE, Jakobovits A. Anti-PSCA mAbs inhibit tumor growth and metastasis formation and prolong the survival of mice bearing human prostate cancer xenografts. Proc Natl Acad Sci U S A. 2001; 98: 2658-63.
34. Vosjan MJ, Perk LR, Visser GW, Budde M, Jurek P, Kiefer GE, et al. Conjugation and radiolabeling of monoclonal antibodies with zirconium-89 for PET imaging using the bifunctional chelate p-isothiocyanatobenzyl-desferrioxamine. Nat Protoc. 2010; 5: 739-43.
35. Lindmo T, Boven E, Cuttitta F, Fedorko J, Bunn PA, Jr. Determination of the immunoreactive fraction of radiolabeled monoclonal antibodies by linear extrapolation to binding at infinite antigen excess. J Immunol Methods. 1984; 72: 77-89.
36. Robinson MK, Doss M, Shaller C, Narayanan D, Marks JD, Adler LP, et al. Quantitative immuno-positron emission tomography imaging of HER2-positive tumor xenografts with an iodine-124 labeled anti-HER2 diabody. Cancer Res. 2005; 65: 1471-8.
37. Sundaresan G, Yazaki PJ, Shively JE, Finn RD, Larson SM, Raubitschek AA, et al. 124I-labeled engineered anti-CEA minibodies and diabodies allow high-contrast, antigen-specific small-animal PET imaging of xenografts in athymic mice. J Nucl Med. 2003; 44: 1962-9.
38. Taschereau R, Vu NT, Chatziioannou AF. Calibration and data standardization of a prototype bench-top preclinical CT. IEEE Nuclear Science Symposium and Medical Imaging Conference. Seattle, WA, USA. Nov 8-15, 2014.
39. Loening AM, Gambhir SS. AMIDE: a free software tool for multimodality medical image analysis. Mol Imaging. 2003; 2: 131-7.
40. Cilliers C, Nessler I, Christodolu N, Thurber GM. Tracking antibody distribution with near-infrared fluorescent dyes: impact of dye structure and degree of labeling on plasma clearance. Mol Pharm. 2017; 17: 757-62.
41. Zhang RR, Schroeder AB, Grudzinski JJ, Rosenthal EL, Warram JM, Pinchuk AN, et al. Beyond the margins: real-time detection of cancer using targeted fluorophores. Nat Rev Clin Oncol. 2017; 14: 347-64.
42. Chi C, Du Y, Ye J, Kou D, Qiu J, Wang J, et al. Intraoperative imaging-guided cancer surgery: from current fluorescence molecular imaging methods to future multi-modality imaging technology. Theranostics. 2014; 4: 1072-84.
43. Cilliers C, Liao J, Atangcho L, Thurber GM. Residualization rates of near-infrared dyes for the rational design of molecular imaging agents. Mol Imaging Biol. 2015; 17: 757-62.
44. Lam JS, Yamashiro J, Shintaku IP, Vessella RL, Jenkins RB, Horvath S, et al. Prostate stem cell antigen is overexpressed in prostate cancer metastases. Clin Cancer Res. 2005; 11: 2591-6.
45. Zhigang Z, Wenlv S. Prostate stem cell antigen (PSCA) expression in human prostate cancer tissues and its potential role in prostate carcinogenesis and progression of prostate cancer. World J Surg Oncol. 2004; 2: 13.
46. Deri MA, Zeglis BM, Francesconi LC, Lewis JS. PET imaging with 89Zr: from radiochemistry to the clinic. Nucl Med Biol. 2013; 40: 3-14.

47. Daneshmand S, Quek ML, Stein JP, Lieskovsky G, Cai J, Pinski J, et al. Prognosis of patients with lymph node positive prostate cancer following radical prostatectomy: long-term results. J Urol. 2004; 172: 2252-5.
48. Li D, Zhang J, Chi C, Xiao X, Wang J, Lang L, et al. First-in-human study of PET and optical dual-modality image-guided surgery in glioblastoma using (68)Ga-IRDye800CW-BBN. Theranostics. 2018; 8: 2508-2520.
49. Lutje S, Heskamp S, Cornelissen AS, Poeppel TD, van den Broek SA, Rosenbaum-Krumme S, et al. PSMA ligands for radionuclide imaging and therapy of prostate cancer: clinical status. Theranostics. 2015; 5: 1388-401.
50. Schwarzenboeck SM, Rauscher I, Bluemel C, Fendler WP, Rowe SP, Pomper MG, et al. PSMA ligands for pet imaging of prostate cancer. J Nucl Med. 2017; 58: 1545-52.